Low Temperature Physics/Fizika Nizkikh Temperatur, 2021, vol. 47, No. 11, pp. 994–1002

Doping from CDW to topological superconductivity: The role of defects on phonon scattering in the non-centrosymmetric Pb_xTaSe_2

A. Glamazda

B. Verkin Institute for Low Temperature Physics and Engineering of the National Academy of Sciences of Ukraine
Kharkiv 61103, Ukraine
E-mail: glamazda@ilt.kharkov.ua

A. Sharafeev, R. Bohle, and P. Lemmens

Institute for Condensed Matter Physics, TU Braunschweig, Braunschweig D-38106, Germany

Laboratory for Emerging Nanometrology, TU Braunschweig, Braunschweig D-38106, Germany

K.-Y. Choi

Department of Physics, Sungkyunkwan University, Suwon, Korea

F. C. Chou and R. Sankar

Institute of Physics, Academia Sinica, Nankang, Taipei 11529, R.O.C. Taiwan

Received August 8, 2021, published online September 24, 2021

The vibrational and electronic properties of the Pb-doped dichalcogenide Pb_xTaSe_2 (x = 0, 0.25, 0.33, 0.5, 0.75, and 1) have been investigated using Raman scattering experiments. A marked variation of the main vibrational modes with Pb concentration x is observed. The concentration dependence of the vibrational modes resembles the dependence of the vibrational modes in $TaSe_2$ on the number of crystallographic layers along the c-axis direction. The temperature and polarization dependences of Raman spectra of Pb_xTaSe_2 revealed additional broad modes in the low-frequency regime, which are discussed in the context of the remnant charge density wave, induced disorder, or PbSe phase formed in the interface of Pb and $TaSe_2$ layers.

Keywords: Raman spectroscopy, topological materials, transition metal dichalcogenides.

1. Introduction

In searching for novel electronic materials two-dimensional (2D) transition metal dichalcogenides (TDMs) with the general MX_2 formula (M = transition metal, X = S, Se, or Te) contribute to the perspective platform of novel hetero-structures [1]. TDMs have the extraordinary physical properties that are caused by the geometrical confinement of the propagation of the quantum excitations and reduction of the screening effects induced in the typical bulk materials. The structural rigidity and intrinsic large mobility inherent to TDMs are necessary preconditions for any potential applications. Besides, the possibilities of doping charge carriers and a large nonlinear electronic response are highly relevant, which could be due to electronic or electron-lattice coupling. Recently, also the importance of spin-orbit interaction and the control of disorder have been highlighted [2]. TDMs show several intriguing features which make them promising materials for spintronics, electronic, and optoelectronics as atomically thin layers are amenable with a defined number of lattice constants. The $TaSe_2$ polytypes are the bright representatives of the TDM family, exhibiting a large number of the charge-density-wave (CDW) ordered structures. The structural simplicity of TDMs also opens a great opportunity to tune the physical properties by modifying the strain and external electric field.

Upon an intercalation of Pb between the $TaSe_2$ layers, CDW is suppressed, and $PbTaSe_2$ shows bulk superconductivity for temperatures below T_c = 3.79 K [3–5]. $PbTaSe_2$ consists of alternating stacking of hexagonal $TaSe_2$ and Pb layers (see Fig. 1) and lacks a center of inversion. The broken inversion symmetry, together with strong spin-orbit

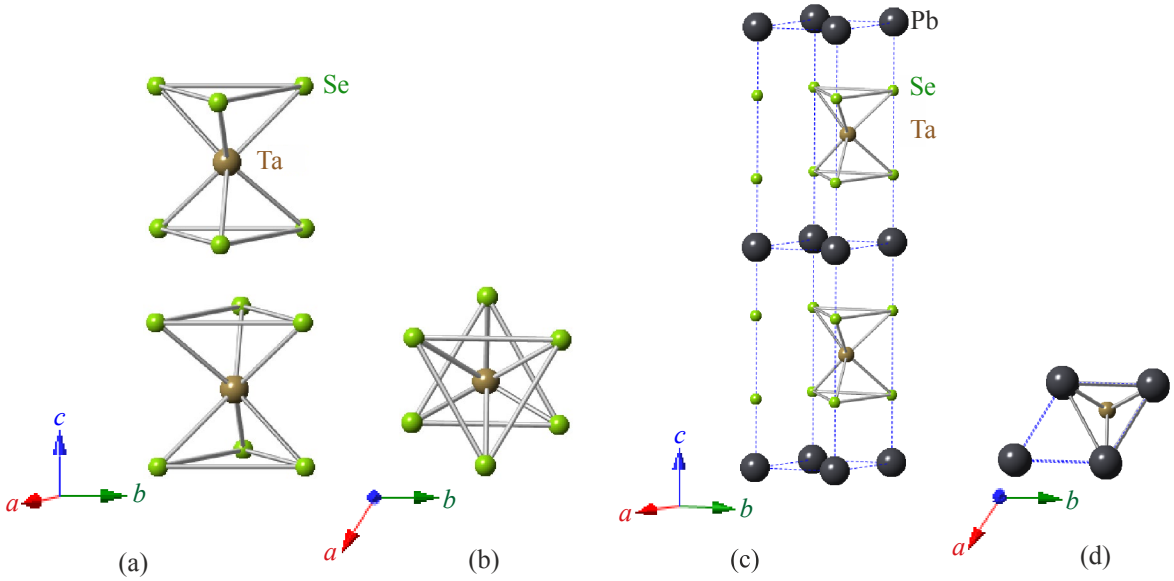

Fig. 1. Sketches of the crystal structure of (a) $TaSe_2$ (hexagonal symmetry), (b) a view along the *c* axis and (c) $PbTaSe_2$ (trigonal D_{3h} symmetry), (d) a view along the *c* axis.

coupling (SOC) linked to the heavy Pb atom, lifts the spin degeneracy of electronic bands and the superconducting states are given by an admixture of spin-singlet and triplet. The Rashba spin splitting amounts to an order of 0.8 eV, which is comparable to that of the giant Rashba semiconductor BiTeI [6]. Noticeably, the injection of Pb into the $TaSe_2$ layers induces distinct structural and electronic changes that have been studied previously. $PbTaSe_2$ hosts topological nodal line states in its bulk electronic structure and topologic Dirac surface states [4, 7, 8]. The confluence of superconductivity and topological bands in a single system allows the study of zero-energy Majorana bound states with non-Abelian statistics that are of relevance for quantum computing [9–11].

As such, it is of great importance to elucidate the role of the Pb layers in determining the structural and electronic properties of Pb_xTaSe_2. Raman spectroscopy is a nondestructive and highly sensitive tool allowing to probe simultaneously lattice and electronic excitations. It has been successfully used to study Raman signatures in topological materials [12–16]. In this paper, we report on detailed Raman scattering measurements of the doped dichalcogenides Pb_xTaSe_2 (x = 0, 0.25, 0.33, 0.5, 0.75, and 1) with focus on tracing structural and electronic properties as a function of Pb concentration. Key observations are the appearance of new, broad peaks in the low-frequency regime, which are not part of symmetry-allowed Raman modes, systematic phonon shifts, as well as a suppression of the CDW features with doping Pb_xTaSe_2

2. Experimental details

Single crystals of $TaSe_2$ and Pb_xTaSe_2 were grown by the chemical vapor transport method [5, 17, 18]. Raman scattering measurements were performed on single crystals of different composition ranging from pure $TaSe_2$ to Pb_xTaSe_2 with x = 0.25, 0.33, 0.5, 0.75, and 1.0 in quasi-backscattering geometry. Light scattering polarizations are given by parallel (*xx*) and cross (*xy*) polarization within the crystallographic *ab* plane. Freshly cleaved sample surfaces were prepared at ambient pressure using scotch tape. Cleaved-off pieces and their opposite faces are quickly cooled down in a vacuum to reduce surface deterioration. The temperature was varied between 8 and 300 K using a closed-cycle cryostat.

As an incident laser excitation, a λ = 532 nm solid state laser and an Ar–Kr-ion multiline gas laser (λ = 476, 488, 514.5, 568, and 647 nm) were used. The laser power was set to P = 5 mW with a spot diameter of approximately 100 μm to avoid heating effects and deterioration of the samples, which were mounted on a sample holder in a vacuum. Six different laser lines allowed to probe the effects of resonance Raman scattering.

Experiments at room temperature were performed using a micro-Raman setup (Horiba LabRAM) with λ = 532 nm. This enabled us to assign the symmetry of phonons, A_{1g} (A') and E_{2g} (E') modes, expected for backscattering geometry. The symbols in brackets correspond to Pb_xTaSe_2. The Raman spectra at low temperatures were collected using a triple Raman spectrometer (Dilor-XY-500) with an attached liquid-nitrogen-cooled CCD (Horiba Jobin-Yvon, Spectrum One CCD-3000V).

3. Experimental results

In Fig. 1, the crystal structures of $TaSe_2$ and $PbTaSe_2$ are depicted. $TaSe_2$ has a layered structure of hexagons that consist of covalently bonded Ta and Se atoms. A plane of Ta atoms is sandwiched between two planes of Se atoms in a trigonal prismatic arrangement. In the

Table 1. Structural parameters and Raman tensors of $TaSe_2$ and $PbTaSe_2$ at room temperature

Compound	Space group	c, Å	Ta–Se dist., Å	Se–Se dist., Å	Raman tensors	Ref.
$TaSe_2$	$P6_3/mmc$	12.7	2.597	3.353	$A_{1g} + 2E_{2g} + E_{1g}$	[21]
	$P\bar{6}m2$	9.35	2.665	3.553	$A' + 3E' + E''$	[22]
$PbTaSe_2$	$P6$	9.35	2.665	3.553	$A' + 3(1E') + 1E'' + 3(2E') + 2E''$	[18]
	$P6_3/mmc$	9.35	2.665	3.553	$A_{1g} + E_{2g} + E_{1g}$	[18]

high-temperature phase, 2H–$TaSe_2$ has a crystal structure of hexagonal (space group $P6_3/mmc$) symmetry. For the $P6_3/mmc$ space group, the irreducible representation of Raman active modes is given by $\Gamma = A_{1g} + 2E_{2g} + E_{1g}$ [19]. We note that E_{1g} modes are not allowed in the measured in-plane polarizations. The crystal structure of Pb_xTaSe_2 is not yet determined. Rather, for $x = 1$, three possibilities have been proposed as listed in Table 1. Trigonal crystal structure D_3h (space group $P\bar{6}m2$) is the most probable, which yields $\Gamma = A' + 3E' + E''$ Raman active modes. The A', E', and E'' are correlated with A_{1g}, E_{2g}, and E_{1g} modes of $TaSe_2$, respectively. The Pb doping leads to only one additional mode with E' symmetry.

3.1. Doping dependence of Raman spectra

Figure 2 shows Raman data of Pb_xTaSe_2 as a function of x. These spectra were collected by the micro-Raman setup. Therefore, their frequency range is limited by a filter that cuts off wavenumbers below 130 cm^{-1}. This means that the suppression of the low-frequency response is due to an instrument artefact by a notch filter. For $x = 0$, we observe two peaks at 236 and 209 cm^{-1} at $T = 300$ K. Our results are in excellent accordance with the data from Ref. 19. As depicted in the inset of Fig. 2, the 209 cm^{-1} mode corresponds to the E^1_{2g} mode involving in-plane stretching motions of the Ta and Se atoms. The 236 cm^{-1} mode is assigned to the out-of-plane vibrations of the Se atoms. We could not detect the anticipated E^2_{2g} mode known as a rigid layer mode due to its very low energy of around 23 cm^{-1} [23].

Upon introducing Pb atoms, a new peak appears at 267 cm^{-1} in addition to the two Raman modes E^1_{2g} (E') and A_{1g} (A') as denoted by the asterisk in the left panel of Fig. 2. The extra mode is tentatively assigned to a 2LO phonon observed in the PbSe nanocrystals [24, 25]. The observed phonons are consistent with the factor group prediction for the $P\bar{6}m2$ space group. Increasing the Pb concentration, the phonon modes, pertaining to $TaSe_2$ sublattice, become narrower and are substantially suppressed. The Raman spectra are fitted to a sum of Lorentzian profiles in order to quantify the evolution of the phonon modes as a function of the Pb content. The resulting phonon parameters are plotted in the right panel of Fig. 2.

With increasing x, the in-plane 209 cm^{-1} mode undergoes a large hardening by 19 cm^{-1}, suggesting a strong impact of the Pb doping on in-plane electronic properties. A close inspection reveals a step-like variation of the frequency with x. This may be related to different Pb ordered phases at low, intermediate and high Pb concentrations. Similar effects have been observed in Na_xCoO_2 with Na ordering [26, 27]. In addition, the drastic suppression of the scattering intensity and a line narrowing occur in the doping range of $x = 0.33$. This is ascribed to screening effects of phonons by electrons in the $TaSe_2$ layer, which become more itinerant through the formation of the Pb layer. This suggests that above $x = 0.33$, the interlayer interaction between the $PbTaSe_2$ layers destabilizes the CDW, which promotes a more metallic behavior in the $TaSe_2$ plane.

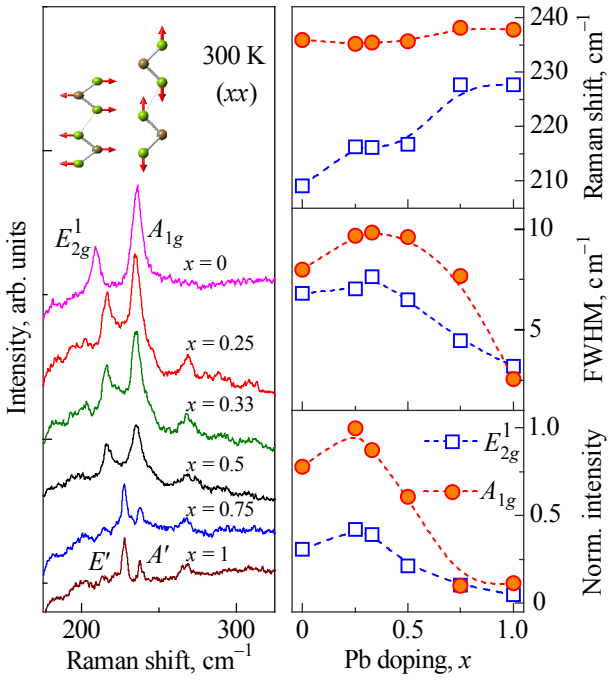

Fig. 2. (Color online) (Left panel) Polarized Raman spectra (xx) of Pb_xTaSe_2 ($x = 0$, 0.25, 0.33, 0.5, 0.75, and 1) measured at room temperature using $\lambda = 532$ nm. Spectra are shifted vertically for clarity. The insets depict the eigenvectors of the 228 and 238 cm^{-1} modes. The relative amplitude of the vibrations is given by the arrows. The green balls stand for the Se atoms, the olive ones for Ta atoms. The asterisk denotes a new phonon at 267 cm^{-1}, which appears upon doping Pb. (Right panel) The frequencies, full widths at half maximum, and integrated intensities of the phonons at 228 and 238 cm^{-1} as a function of Pb doping.

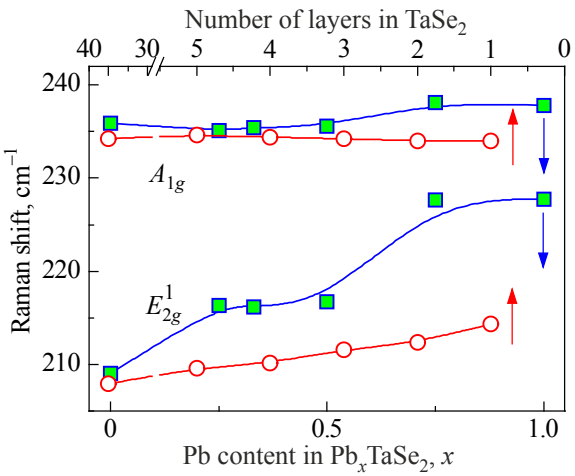

Fig. 3. Comparison of phonon frequency vs. the number of layers (open circles and top axis, respectively) in exfoliated $TaSe_2$ [19] and phonon frequency vs. Pb concentration (filled squares and bottom axis, respectively) in bulk single crystals of Pb_xTaSe_2.

To analyze further the influence of the Pb layer on the electronic properties, the x dependence of the frequencies of the E^1_{2g} and A_{1g} modes is compared with their frequencies as a function of the number of layers corresponding to the thickness of exfoliated crystals in Fig. 3 [19]. Overall, the A_{1g} mode varies little with x and thickness. The observed phonon shift is an order of 1 cm^{-1}. This is contrasted by the mode, which hardens by 19 cm^{-1} with increasing x for Pb_xTaSe_2 and by 5 cm^{-1} with increasing number of layers in the exfoliated crystals [19]. Here we stress that Pb doping exerts a much stronger impact on the electric properties than the thickness variation. Obviously, this is linked to the interfacial effect between the graphene-like Pb and the superconducting $TaSe_2$ layers, which is absent for the exfoliated $TaSe_2$ sample.

3.2. Temperature-induced effects in Pb_xTaSe_2

Let us turn to the temperature dependence of Raman spectra of Pb_xTaSe_2 (x = 0, 0.33, and 1), shown in Fig. 4. For temperatures $T > T_{ICDW}$ = 123 K, $TaSe_2$ exhibits a broad maximum at around ~ 140 cm^{-1} in addition to the two phonon modes discussed above. The former has been attributed to two-phonon Raman scattering amplified by anharmonicity in systems with a Kohn anomaly [23, 28]. In the temperature range between T_{ICDW} and T_{CCDW}, the two-phonon scattering evolves to a quasielastic response. Below T_{CCDW} = 90 K, a number of sharp, well-defined Raman modes at 46, 63, and 81 cm^{-1} appear. They are linked to the CDW $3a\times3a\times c$ superlattice [23, 28]. As to Pb_xTaSe_2 (x = 0.33 and 1), the broad maxima at 40, 80, and 135 cm^{-1} are present in the whole measured temperature range while the background is being suppressed with decreasing temperature [see Figs. 4(b) and 4(c)]. Their assignment will be given below.

In Fig. 5, we summarize the temperature dependence of the frequency, the linewidth and intensity for $TaSe_2$. Both E^1_{2g} and A_{1g} modes show a distinct change through T_{CCDW} and T_{ICDW}. In particular, the linewidth appreciably decreases and the intensity increases steeply upon cooling through T_{CCDW}. This is due to the partial depletion of electronic states at the Fermi surface, which leads to a weakening of charge screening effects.

Let us discuss the temperature dependences of the phonon modes and the background scattering for $PbTaSe_2$, which is summarized in Figs. 6 and 7. The phonon frequency hardens by 3–5 cm^{-1} with lowering temperature.

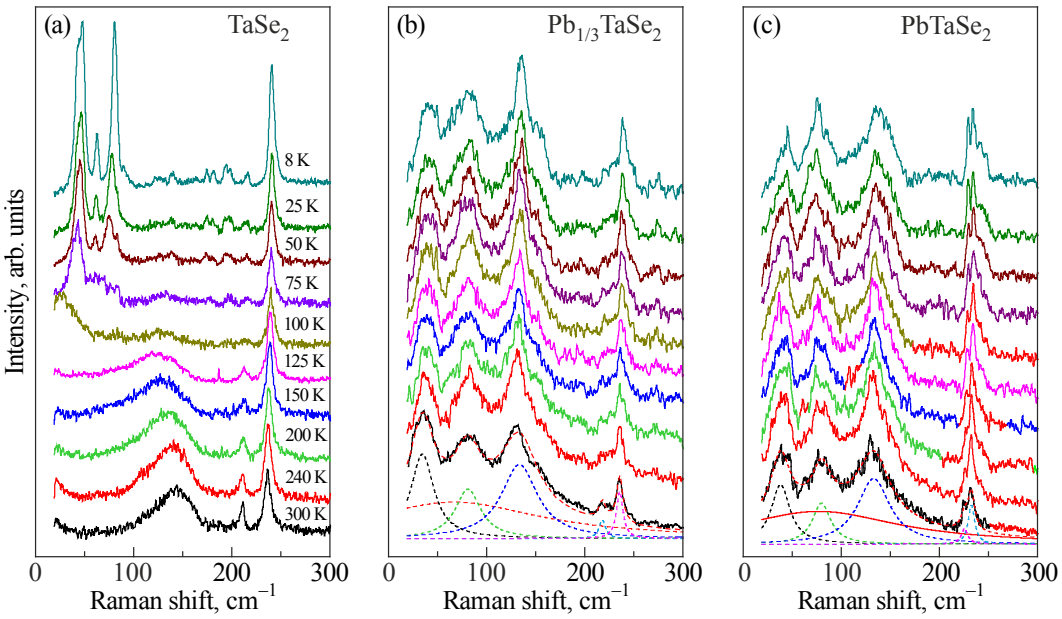

Fig. 4. Polarized Raman spectra of $TaSe_2$ (a), $Pb_{1/3}TaSe_2$ (b) and $PbTaSe_2$ (c) in xx polarization with different temperatures from 300 to 8 K. The Raman spectra are offset for clarity. The dashed lines represent a fit of phonon modes together with a background.

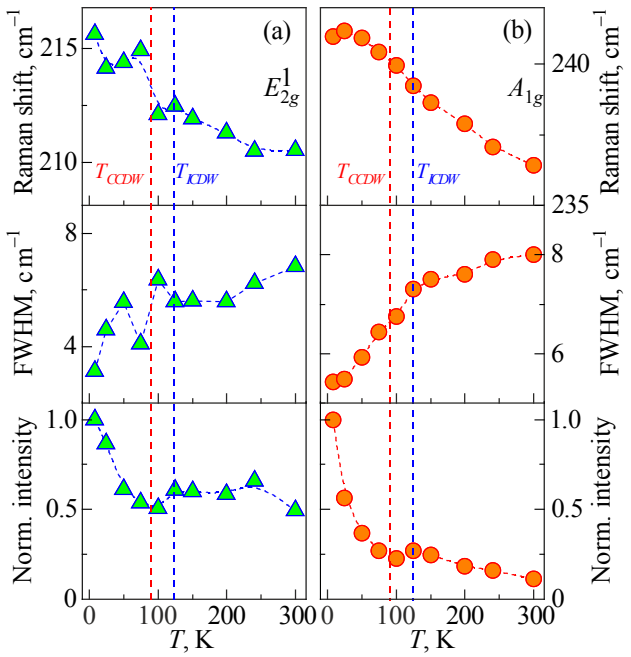

Fig. 5. Temperature dependences of the frequency, the linewidth and intensity of $TaSe_2$ phonons for (a) E^1_{2g} and (b) A_{1g} intrinsic modes, respectively. The dashed lines denote the incommensurate CDW and commensurate phase transition temperatures T_{ICDW} = 123 K and T_{CCDW} = 90 K, respectively. The phonon intensities were corrected by the Bose factor.

This is explained by anharmonicities in the lattice potential energy as commonly observed, e.g., in MoS_2 and graphene [29]. This is comparable to the change in frequency, $\Delta\omega$ = = 4.5 cm^{-1}, of $TaSe_2$. The FWHM of the in-plane E' and

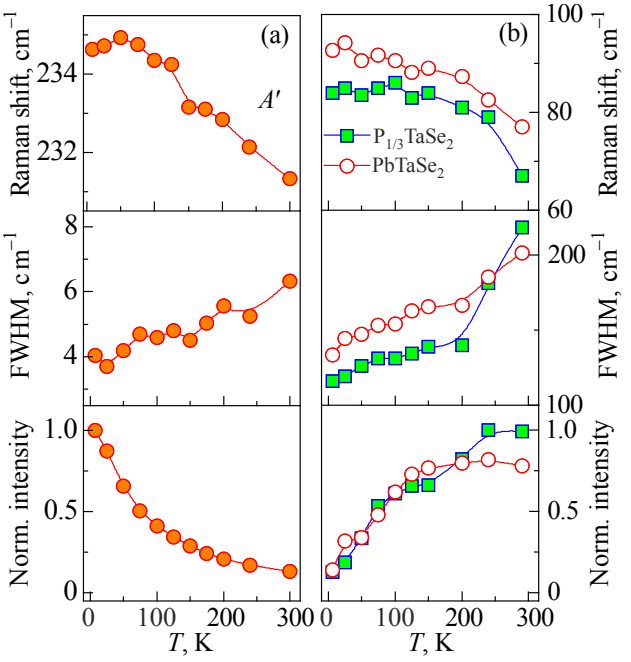

Fig. 6. Temperature dependences of the frequency, the linewidth and intensity of $PbTaSe_2$ for (a) E' (Pb–Pb) mode at 136 cm^{-1} and (b) E' mode at 230 cm^{-1}, respectively. The phonon intensities were corrected by the Bose factor.

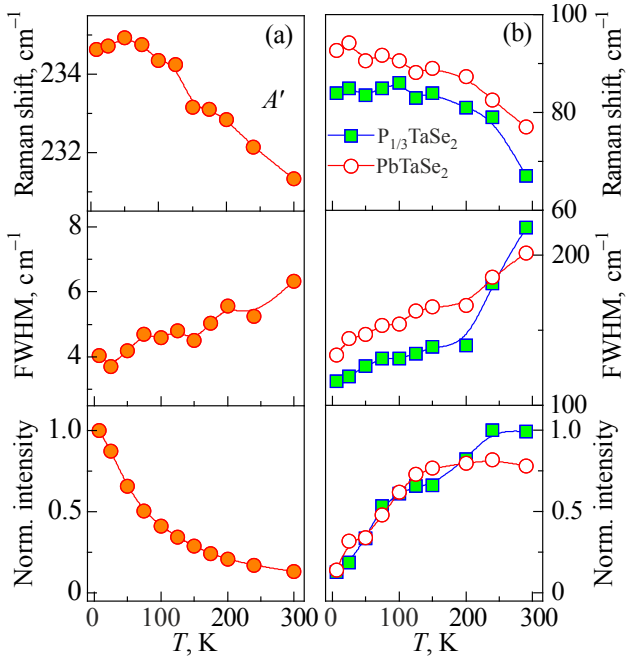

Fig. 7. Temperature dependences of the frequency, the linewidth and intensity of $PbTaSe_2$ for (a) A' mode and (b) the background signal. The phonon intensities were corrected by the Bose factor but the background intensity consists of raw data.

A' modes of $PbTaSe_2$ is smaller than that of the respective modes of $TaSe_2$. The change of the FWHM over a temperature range of T = 8–300 K amounts to $\Delta\Gamma \approx$ 1–2 cm^{-1} for $PbTaSe_2$ and $\Delta\Gamma \approx$ 5.7 cm^{-1} for $TaSe_2$. No discernible anomaly can be found in the temperature dependence of the FWHM. In contrast, the E' (Pb–Pb) mode exhibits a large width and a step-like decrease of the FWHM between 100 and 150 K [see Fig. 6(a)]. At the respective temperature, the integrated intensity increases steeply. The same trend is visible for the E' and A' modes as well. Furthermore, we would like to draw attention to the temperature dependence of the background scattering. As evident from Fig. 7(b), the background signal decreases substantially for temperatures below 150 K. Most probably, the background response originates from light scattering of electrons by Pb defects.

Combining the above findings, it seems that the charge dynamics of the hybrid Pb and $TaSe_2$ layers is different from that of the pure $TaSe_2$ layers. Topologically protected materials show coherent surface states at low temperatures whereas incoherent dynamics becomes dominant due to thermally excited phonons at high temperatures [30]. In our case, phonons mediate the Pb and $TaSe_2$ layers, thereby changing the charge dynamics upon heating. This may explain the appearance of the background scattering by Pb defects and phonons at high temperatures and the phonon anomalies of the E' (Pb–Pb) mode.

3.3. Resonance effects

We performed resonance Raman scattering measurements on $PbTaSe_2$ with six different laser wavelengths.

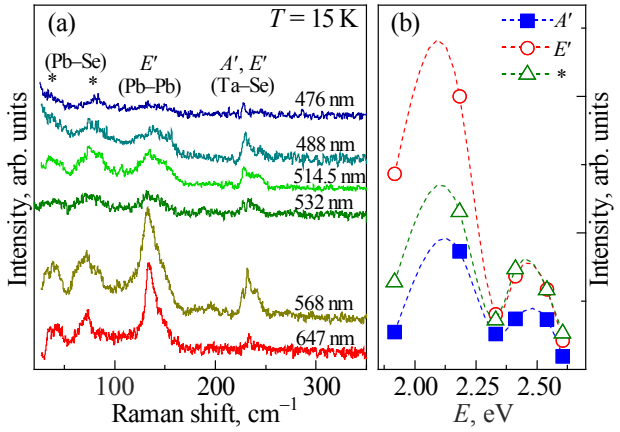

Fig. 8. (a) Raman spectra of $PbTaSe_2$ with different incident laser excitations measured in *xx* polarization and at $T = 15$ K. (b) Laser wavelength dependences of the intensity of the E', A' and modes marked with '∗'. The asterisks denote phonon modes related to PbSe nanocrystals. The symbols denote experimental points and the broken curves represent B-spline fit drawn to guide the eye.

Respective data and analysis of the intensity are shown in Figs. 8(a) and 8(b). A resonance effect of the Raman intensity is expected if the incident photon energy matches the energy of respective electronic transitions. In $PbTaSe_2$, the phonon modes indeed show a strong resonance effect in intensity with a maximum at 568 nm (2.18 eV). A sharp minimum is observed at 647 nm (1.92 eV). The largest magnitude of the resonance effect has the E' (Pb–Pb mode) line, for instance $I_{568}/I_{532} \approx 5$, whereas for the A' mode and for the modes marked with '*' this intensity ratio is $I_{568}/I_{532} \approx 3.3$. The lone-pair *p*-electron states of Pb with their high polarizability are a possible reason for this enhancement.

In Fig. 9, polarization-dependent Raman spectra of $PbTaSe_2$ are shown. The A' out-of-plane vibrational mode is suppressed in crossed (*xy*) polarization, while the E' in-plane vibrational mode remains unaltered, as expected from the selection rules. The broad mode at ~ 40 cm^{-1} exhibits little polarization dependence, whereas the other two

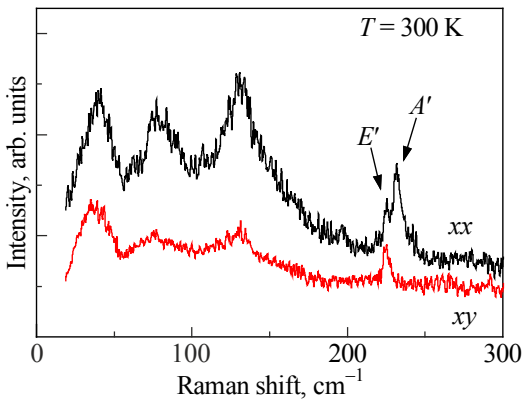

Fig. 9. Polarization dependences of Raman spectra of $PbTaSe_2$ at $T = 300$ K in *xx* and *xy* polarizations.

broad modes around 80 and 130 cm^{-1} show sizable changes. However, we cannot identify apparent selection rules of the low-energy broad peaks. This indicates that they are related to disorders or defects induced by Pb intercalation. This effect will be described in details below.

4. Discussion

In the first part of the discussion, the relation of properties such as the thickness of $TaSe_2$ layered compound, Pb concentration in Pb_xTaSe_2 and the covalency of the Ta–Se bond will be considered and related to interlayer and intralayer interactions and their effect on the phonon frequencies. In the second part, we consider different possible origins for the low-frequency broad modes, which appear upon Pb intercalation into $TaSe_2$. We assume that such phenomena could be related to the remnants of CDW phase in the Pb-doped compounds, or induced disorder and defects, or the formation of PbSe nanocrystals.

For atomically thin, exfoliated layers of $TaSe_2$ and MoS_2, a 3 % hardening of the E_{2g} modes and a very weak softening of the A_{1g} have been observed with decreasing thickness. The latter corresponds to a decreasing number of unit cells [19, 31]. However, in a classical model of coupled harmonic oscillators, a hardening of phonon modes is expected only with increasing coupling. The opposite effect in the experiments points to an additional interaction which is supposed to be a long-range Coulomb interaction from a charge transfer between the layers.

This apparent contradiction also exists for Pb_xTaSe_2 with an even more pronounced 10% hardening of the E_{2g} phonon with increasing Pb concentration. The geometric changes of Pb_xTaSe_2 with increasing *x* can be summarized as an increase in the layer distance, its thickness, the distance between Ta and Se atoms, and the Se–Ta–Se angle. We assume that they reflect a change in the electronic configuration and bonding induced by Pb intercalation and, in their turn, the induced charge in the layer. The formal oxidation states of Ta and Se in $TaSe_2$ are +4 and –2. With full Pb intercalation, the Ta valence changes to +2. This reduction decreases ionic interactions and increases covalent bonding contributions. The Ta–Se interaction shows a bigger effect, while the Se–Se mode is largely unchanged. The insensitivity of the A_{1g} mode to the Pb intercalation may be due to the fact that van der Waals (VdW) and long-range Coulomb interactions are compensated by charge dynamics. It is worth mentioning that such interplay of long-range Coulomb interactions between chalcogen atoms and metals together with VdW forces is also discussed for GaS [32] and GaSe [33].

Next, we focus on doped Pb_xTaSe_2 samples and broad modes at low frequencies. First, we propose that after intercalation of the Pb layer between Ta–Se layers, the CDW modes could remain afterwards. In Fig. 4, one can see that the frequencies of the two highly intense CDW modes from $TaSe_2$ are similar to the ones in Pb_xTaSe_2 (at about 40 and 80 cm^{-1}).

Nevertheless, resistivity measurements [4] unveil the absence of CDW in the compound. Similar investigations were done also for copper-intercalated superconductor Cu_xTiSe_2. Titanium diselenide is a CDW material with $T_{CDW} = 200$ K and upon Cu doping, this compound becomes superconducting with $T_c = 4.15$ K [34]. A Raman scattering study shows that the E_g and A_{1g} CDW amplitude modes are heavily suppressed with concentration of Cu of 5 % and the CDW phase is not present anymore.

However, there are cases when the phase transition temperature of a CDW state increases with certain doping. This is the case for $IrTe_{2-x}Se_x$ [35]. Also, it is worthwhile to mention that the change of the Ta oxidation state to +2, introducing two electrons to Pb_xTaSe_2, may also lead to some phase separation or charge modulation. Such a short-range order assumes a partial localization of these states that are not available for transport. Further studies are needed to clarify this situation and to evaluate whether these states play a role in enhancing the superconducting transition temperature.

In this section, we discuss arguments against a residual CDW in the doped samples. We focus on the broad feature around 130 cm^{-1}, consisting of a broad mode and superimposed sharp mode (Pb–Pb interaction [36]). Very likely, the broad mode could be assigned to a second-order Raman process, since a similar peak is observed in $TaSe_2$. In accordance Raman measurements of transition metal dichalogenides, the 2-phonon Raman mode has different temperature dependence in comparison with $PbTaSe_2$ [23]. Normally, 2-phonon Raman scattering is strongly suppressed with decreasing temperatures, and the peak shifts towards lower energies. This process is distinctive for CDW-type materials, such as $TaSe_2$ and $NbSe_2$ [37]. Nevertheless, in $PbTaSe_2$ the behavior of the broad mode is different compared to the usual 2-phonon mode in transition metal dichalcogenides. In our case, the broad mode at ~ 130 cm^{-1} in $PbTaSe_2$ is not suppressed at low temperatures. Such behavior is incompatible with a CDW scenario.

A second possible explanation for the broad modes at 40, 80, and 135 cm^{-1} is related to a structural transition due to intercalation. Upon Pb doping, the crystal structure changes drastically. For instance, the layers of Ta and Se atoms in $TaSe_2$ form a "star" along the c axis and have an inversion center (see Fig. 1). However, after intercalation of Pb atoms into the structure, such formation is triangular, leading to a non-centrosymmetric system having no more inversion center. Due to this process, besides Ta–Se Raman modes, one could observe additional modes possibly from Pb–Pb or/and Pb–Se interaction.

There is another perspective related to a possible formation of Pb clusters. Spiro *et al.* [36] performed Raman measurements on $Pb_6O(OH)_6^{4+}$ containing Pb clusters. They observed several modes related to Pb–Pb interactions. The Raman frequency of such interactions depends on the distance between Pb atoms. An intense and sharp peak at 150 cm^{-1} in $Pb_6O(OH)_6^{4+}$ has been attributed to an interaction of Pb atoms at a distance of 3.44 Å, which is, in fact, the anticipated distance between Pb atoms in $PbTaSe_2$. In this respect, the 130 cm^{-1} mode observed in $PbTaSe_2$ may be due to Pb–Pb clustering. As Pb atoms can have different positions in the clusters with a variation of distances, other broad modes could have the same origin. In $Pb_6O(OH)_6^{4+}$ there also exist broader modes at low frequencies that superimpose sharper excitations [36].

The third reason for the appearance of these broad modes is provided by the formation of PbSe nanocrystals or Pb–Se bondings. The polarized Raman scattering experiments showed that the A' and E' vibrational modes follow the selection rules (Fig. 8). However, the additional broad modes have little difference between the xx and xy polarizations. When Pb atoms are inserted between the $TaSe_2$ layers, predominantly Pb atoms form a Pb layer by Pb–Pb bonding. Nonetheless, it is possible that they form PbSe nanocrystals through Pb–Se bonding. Indeed, lead chalcogenides PbX (X = S, Se, or Te) are stable semiconductors and their Raman spectra are scattered between 30 and 130 cm^{-1} with second-order scattering observed at about 260 cm^{-1} [24, 25]. This accounts for the first-order peaks at 40, 80, and 135 cm^{-1}, as well as the second-order peak 267 cm^{-1}, which are denoted by the asterisks in Figs. 2 and 8. Such a scenario provides an explanation for their obscure polarization and temperature dependence distinctly different from the E' (Pb–Pb) mode, E' and A' modes. Therefore, we conclude that doping $TaSe_2$ with Pb atoms forms a heterogeneous Pb–Se bonding in addition to the Pb layer.

5. Conclusion

To conclude, systematic Raman scattering experiments have been performed in Pb_xTaSe_2 as function of Pb content x = 0, 0.25, 0.33, 0.5, 0.75, and 1. With the crossover of CDW to topological superconductivity, Raman spectra showed a pronounced hardening of the in-plane E_{2g} mode with increasing Pb content, which is much larger than an effect observed in exfoliated crystals with different layer thickness. This can be taken as a signature of nontrivial coupling between Pb and $TaSe_2$ layers, which is responsible for structural and electronic changes. Additional broader low-frequency modes based on both intrinsic and extrinsic origins and their effect on the electronic structure of Pb_xTaSe_2 were discussed.

We are grateful to V. Gnezdilov, Yu. G. Pashkevich, and A. Möller for an important discussion. This research was funded by the DFG Excellence Cluster Quantum-Frontiers, EXC 2123-390837967 and DFG Le967/16-1. RS acknowledges the financial support provided by the Ministry of Science and Technology in Taiwan under project number MOST-110-2112-M-001-065-MY3 and Academia Sinica for the budget of AS-iMATE-109-13. KYC was supported by the National Research Foundation (NRF) of Korea (Grants No. 2020R1A2C3012367).

1. S. Husain, R. Gupta, A. Kumar, P. Kumar, N. Behera, R. Brucas, S. Chaudhary, and P. Svedlindh, *Appl. Phys. Rev.* **7**, 041312 (2020).
2. M. Xu, T. Liang, M. Shi, and H. Chen, *Chem. Rev.* **113**, 3766 (2013).
3. M. N. Ali, Q. D. Gibson, T. Klimczuk, and R. J. Cava, *Phys. Rev. B* **89**, 020505(R) (2014).
4. Cheng-Long Zhang, Zhujun Yuan, Guang Bian, Su-Yang Xu, Xiao Zhang, M. Zahid Hasan, and Shuang Jia, *Phys. Rev. B* **93**, 054520 (2016).
5. T. Le, Y. Sun, H.-K. Jin, L. Che, L. Yin, J. Li, G. Pang, C. Xu, L. Zhao, S. Kittaka, T. Sakakibara, K. Machida, R. Sankar, H. Yuan, G. Chen, X. Xu, S. Li, Y. Zhou, and X. Lu, *Science Bulletin* **65**, 1349 (2020).
6. K. Ishizaka, M. S. Bahramy, H. Murakawa, M. Sakano, T. Shimojima, T. Sonobe, K. Koizumi, S. Shin, H. Miyahara, A. Kimura, K. Miyamoto, T. Okuda, H. Namatame, M. Taniguchi, R. Arita, N. Nagaosa, K. Kobayashi, Y. Murakami, R. Kumai, Y. Kaneko, Y. Onose, and Y. Tokura, *Nat. Mater.* **10**, 521 (2011).
7. G. Bian, T.-R. Chang, R. Sankar, S.-Y. Xu, H. Zheng, T. Neupert, C.-K. Chiu, S.-M. Huang, G. Chang, I. Belopolski, D. S. Sanchez, M. Neupane, N. Alidoust, C. Liu, B. Wang, C.-C. Lee, H.-T. Jeng, C. Zhang, Z. Yuan, S. Jia, A. Bansil, F. Chou, H. Lin, and M. Z. Hasan, *Nat. Commun.* **7**, 10556 (2016).
8. T.-R. Chang, P.-J. Chen, G. Bian, S.-M. Huang, H. Zheng, T. Neupert, R. Sankar, S.-Y. Xu, I. Belopolski, G. Chang, B. Wang, F. Chou, A. Bansil, H.-T. Jeng, H. Lin, and M. Z. Hasan, *Phys. Rev. B* **93**, 245130 (2016).
9. S.-Y. Guan, P.-J. Chen, M.-W. Chu, R. Sankar, F. Chou, H.-T. Jeng, C.-S. Chang, and T.-M. Chuang, *Sci. Adv.* **23**, e1600894 (2016).
10. S. S. Zhang, J.-X. Yin, G. Dai, L. Zhao, T.-R. Chang, N. Shumiya, K. Jiang, H. Zheng, G. Bian, D. Multer, M. Litskevich, G. Chang, I. Belopolski, T. A. Cochran, X. Wu, D. Wu, J. Luo, G. Chen, H. Lin, F.-C. Chou, X. Wang, C. Jin, R. Sankar, Z. Wang, and M. Z. Hasan, *Phys. Rev. B* **101**, 100507(R) (2020).
11. T. Ideue, S. Koshikawa, H. Namiki, T. Sasagawa, and Y. Iwasa, *Phys. Rev. Research* **2**, 042046(R) (2020).
12. G. B. Osterhoudt, Y. Wang, C. A. C. Garcia, V. M. Plisson, J. Gooth, C. Felser, P. Narang, and K. S. Burch, *Phys. Rev. X* **11**, 011017 (2021).
13. D. Wulferding, P. Lemmens, F. Bscher, D. Schmeltzer, C. Felser, and Ch. Shekhar, *Phys. Rev. B* **102**, 075116 (2020).
14. D. Wulferding, Y.-S. Choi, S.-H. Do, Ch. H. Lee, P. Lemmens, C. Faugeras, Y. Gallais, and K.-Y. Choi, *Nat. Commun.* **11**, 1603 (2020).
15. K. Kataoka, D. Hirai, T. Yajima, D. Nishio-Hamane, R. Ishii, K.-Y. Choi, D. Wulferding, P. Lemmens, S. Kittaka, T. Sakakibara, H. Ishikawa, A. Matsuo, K. Kindo, and Z. Hiroi, *J. Phys. Soc. Jpn.* **89**, 114709 (2020).
16. A. Sharafeev, V. Gnezdilov, R. Sankar, F. C. Chou, and P. Lemmens, *Phys. Rev. B* **95**, 235148 (2017).
17. R. Sankar, G. N. Rao, I. P. Muthuselvam, G. Bian, H. Zheng, G. P.-J. Chen, T.-R. Chang, S. Xu, G. S. Murgan, C.-H. Lin, W.-L. Lee, H.-T. Jeng, M. Z. Hasan, and F.-C. Chou, *Single crystal growth and physical property characterization of $PbTaSe_2$ as a noncentrosymmetric type-II superconductor* (2015), arXiv:1511.05295 [cond-mat.supr-con].
18. Y.-J. Long, L.-X. Zhao, P.-P. Wang, H.-X. Yang, J.-Q. Li, H. Zi, Z.-A. Ren, C. Ren, and G.-F. Chen, *Chinese Phys. Lett.* **33**, 037401 (2016).
19. P. Hajiyev, C. Cong, C. Qiu, and T. Yu, *Sci. Rep.* **3**, 2593 (2013).
20. W. Zhao, Z. Ghorannevis, K. K. Amara, J. R. Pang, M. Toh, X. Zhang, C. Kloc, P. H. Tan, and G. Eda, *Nanoscale* **5**, 9677 (2013).
21. E. Z. Kuchinskii, I. A. Nekrasov, and M. V. Sadovskii, *J. Exp. Theor. Phys.* **114**, 671 (2012).
22. R. Eppinga and G. Wiegers, *Physica B+C* **99**, 121 (1980).
23. S. Sugai, K. Murase, S. Uchida, and S. Tanaka, *Physica B+C* **105**, 405 (1981).
24. J. Habinshuti, O. Kilian, O. Cristini-Robbe, A. Sashchiuk, A. Addad, S. Turrell, E. Lifshitz, B. Grandidier, and L. Wirtz, *Phys. Rev. B* **88**, 115313 (2013).
25. C. Gayner and K. K. Kar, *J. Appl. Phys.* **117**, 103906 (2015).
26. A. Donkov, M. M. Korshunov, I. Eremin, P. Lemmens, V. Gnezdilov, F. C. Chou, and C. T. Lin, *Phys. Rev. B* **77**, 100504 (2008).
27. T. Wu, K. Liu, H. Chen, G. Wu, Q. L. Luo, J. J. Ying, and X. H. Chen, *Phys. Rev. B* **78**, 115122 (2008).
28. E. F. Steigmeier, G. Harbeke, H. Auderset, and F. J. DiSalvo, *Solid State Commun.* **20**, 667 (1976).
29. S. Sahoo, A. P. S. Gaur, M. Ahmadi, M. J.-F. Guinel, and R. S. Katiyar, *J. Phys. Chem. C* **117**, 9042 (2013).
30. A. A. Reijnders, Y. Tian, L. J. Sandilands, G. Pohl, I. D. Kivlichan, S. Y. F. Zhao, S. Jia, M. E. Charles, R. J. Cava, N. Alidoust, S. Xu, M. Neupane, M. Z. Hasan, X. Wang, S. W. Cheong, and K. S. Burch, *Phys. Rev. B* **89**, 075138 (2014).
31. C. Lee, H. Yan, L. E. Brus, T. F. Heinz, J. Hone, and S. Ryu, *ACS nano* **4**, 2695 (2010).
32. N. Kuroda and Y. Nishina, *Phys. Rev. B* **19**, 1312 (1979).
33. T. J. Wieting and J. L. Verble, *Phys. Rev. B* **5**, 1473 (1972).
34. H. Barath, M. Kim, J. F. Karpus, S. L. Cooper, P. Abbamonte, E. Fradkin, E. Morosan, and R. J. Cava, *Phys. Rev. Lett.* **100**, 106402 (2008).
35. A. Glamazda, K.-Y. Choi, P. Lemmens, J. J. Yang, and S.-W. Cheong, *New J. Phys.* **16**, 093061 (2014).
36. T. G. Spiro, V. A. Maroni, and C. O. Quicksall, *Inorg. Chem.* **8**, 2524 (1969).
37. Y. Wu, M. An, R. Xiong, J. Shi, and Q. M. Zhang, *J. Phys. D: Appl. Phys.* **41**, 175408 (2008).

Легування від CDW до топологічної надпровідності: роль дефектів у розсіюванні фононів у нецентросиметричному Pb_xTaSe_2

A. Glamazda, A. Sharafeev, R. Bohle, P. Lemmens, K.-Y. Choi, F. C. Chou, R. Sankar

Обговорюються результати раманівських досліджень коливальних та електронних властивостей легованого Pb дихаль-когеніду Pb_xTaSe_2 (x = 0, 0,25, 0,33, 0,5, 0,75 та 1). Виявлено помітну зміну основних коливальних раманівських мод в залежності від концентрації Pb. Концентраційна залежність коливальних мод демонструє схожість з поведінкою коливальних мод в раманівських спектрах $TaSe_2$ в залежності від кількості кристалографічних шарів уздовж напрямку осі c. Проведений аналіз залежності раманівських спектрів Pb_xTaSe_2 від температури та поляризації виявив додаткові широкі моди в низькочастотному діапазоні, які можуть бути обумовлені наявністю залишкової хвилі густини заряду, індукованого безладу або PbSe фази, що утворюється на межі поділу шарів Pb та $TaSe_2$.

Ключові слова: раманівська спектроскопія, топологічні матеріали, дихалькогеніди перехідних металів.